We are IntechOpen, the world's leading publisher of Open Access books Built by scientists, for scientists

4,800
Open access books available

122,000
International authors and editors

135M
Downloads

Our authors are among the

154
Countries delivered to

TOP 1%
most cited scientists

12.2%
Contributors from top 500 universities

WEB OF SCIENCE™

Selection of our books indexed in the Book Citation Index in Web of Science™ Core Collection (BKCI)

Interested in publishing with us?
Contact book.department@intechopen.com

Numbers displayed above are based on latest data collected.
For more information visit www.intechopen.com

Chapter 2

Biomimetic Sensors for Rapid Testing of Water Resources

Jill M. Grimme and Donald M. Cropek

Additional information is available at the end of the chapter

http://dx.doi.org/10.5772/52438

1. Introduction

Environmental monitoring is a critical mission of the U. S. Army Corps of Engineers due to its commitment to support not only the soldiers, but also to maintain the environment on military lands and installations. The detection of contaminants present in the environment, specifically water resources, is vital to ensure the safety of soldiers at forward base locations and to promote the sustainable usage of military lands. Therefore, fieldable, robust, and sensitive detection mechanisms are required for screening applications that provide rapid environmental assessment. Typically, sensor and detector research focuses on new techniques and methods to characterize a sample for an analyte of interest. A metric that must be satisfied for success is the selectivity of the sensor, i.e., how well it can measure only a particular analyte without response to other closely related chemicals. Under certain conditions, it makes sense to use sensors with specificity. However, a quantitative result alone does not translate easily to a measure of toxicity to the soldier or to an assessment of environmental impact. Further, the uncertainties inherent to unfamiliar and frequently hostile environments preclude exact knowledge of a complete set of potential analytes.

Our Biomimetic Sensor for Rapid Testing of Water Resources program at the Construction Engineering Research Laboratory (ERDC-CERL) was initiated precisely to investigate and advance aspects of miniaturized microfluidic devices for toxicity sensing. This work package represents a change in the sensor and detector paradigm typical of legacy Corps of Engineer analytical research. Providing the soldier in the military environment with a rapid, universal indicator of a chemical threat may prove more powerful and vital than identifying what compound is present. Our goal in this program was to assess the property of overall toxicity, rather than acquisition of a compendium of individual chemical concentrations. The chosen way to acquire this property was to expose the water sample of interest to a population of

living cells where we ascertain the harmful impact of the sample on cellular metabolism, function and communication.

Most commercially available rapid toxicity screening test kits use luminescent bacteria, photosynthetic algae, or plant enzymes to monitor toxicity via luminescence or colorimetric assay, which report a decrease in cellular respiration or enzyme turnover in relation to the toxicity of the test sample (http://www.epa.gov/nrmrl/std/etv/vt-ams.html#rtts). From a soldier health perspective, however, the use of mammalian (human) cell-based biosensors for rapid risk assessments would be more beneficial due to the direct correlation of the toxicity data to the human health effects on the soldiers. Therefore, many of the sensing mechanisms we are developing integrate more biorelevant cells for specific major organ systems into the sensing platform. Further, we maintain a more ambitious goal to move beyond homogeneous cell culture to an intelligently designed heterogeneous population of multiple cell types that recapitulates *in vivo* tissue function. Depending on the final application however, these same sensor platforms could be populated with fish and animal cells/tissues when direct environmental impact analyses are required on particular strata of an ecosystem.

Cell-based biosensors utilize immobilized living cells (either prokaryote or eukaryote) as the biorecognition element. The impact of the chemical stimulus on the cell generates changes to the intracellular or extracellular biochemistry that are most frequently detected either electrically or optically [1, 2]. While the cellular response may require an incubation time with the contaminant that increases total analysis time, the ability of cells to respond to minute changes in their complex environment imbues cell-based biosensors with high sensitivity and more importantly for our task, biorelevance. Also, the ability of the biosensor to report the bioavailability of a compound may be more critical than the analytical determination that the compound is present. Unlike some current biorecognition based sensors that utilize antibodies, aptamers, or other analyte-specific binding mechanisms, biosensors incorporating intact living cells can respond to emerging or little known chemical or biological threats and can be engaged as broad spectrum screening tools [1]. Finally, by exploiting the biochemical response of the living cell to the entire complex composition of a water sample, we can ascertain additive and synergistic effects impossible to discern using a suite of selective sensors.

Despite the advantages of using cell-based biosensors, there are non-trivial obstacles to consider when incorporating living cells onto a device to be used in austere environments. Perturbations in temperature, pH, oxygen/carbon dioxide levels, nutrients, and sterility can all have deleterious effects on the survivability of the cell population thus rendering the biosensor less reliable or simply unusable. Therefore, maintaining a well-defined and healthy cell population with adequate controls presents the most difficult challenge for the development and wide spread usage of cell-based biosensors.

Recognizing these hurdles, we formed a collaborative research effort that aimed to create sensors that instantly alert personnel to a toxic threat in water by designing, building, and testing microfluidic devices that accurately replicate the physiological response of an organ structure to contaminants in water. We are developing both electrical and optical transduction methods for the detection and translation of the cell's physiological response to a water toxicant. The ultimate goal of the project was the development of a microfluidic platform that

http://dx.doi.org/10.5772/52438

housed a complete set of three-dimensional (3D) "organs" reconstructed from heterogeneous cell/tissue populations that worked in a physiologically realistic manner to represent the circulatory pattern of an entire organism (*e.g.*, human). With the understanding that recapitulating a truly physiologically accurate "body on a chip" is a momentous task, we have focused our research efforts to develop tools, technology and scientific knowledge that bring us closer to this vision. This chapter describes several of the resultant scientific collaborations with academic partners in this biomimetic sensor program.

A class of *in vitro* tissue models known as micro-cell culture analogs (μCCAs) has been developed by pioneering research in the laboratory of Dr. Michael Shuler at Cornell University [3-5]. Micro-CCAs are composed of a microfluidic platform that allows multiple "organs" to be combined in a physiologically realistic manner. Such a device is a tangible representation of a physiologically based pharmacokinetic (PBPK) model that translates *in vivo* conditions such as liquid to cell ratios, fluid residence times, and physiological shear stress that are realistic to each organ type into parameters that can be integrated into a microfluidic device through microfabrication. Therefore, each organ is recreated on the chip with cells housed in a precisely designed organ chamber [6] (Figure 1). The evolutionary design of the μCCA has increased from three chambers [5], to four chambers [7] and includes more complex organs and tissue types such as fat cells, which may alter the response [8]. Additionally, one of the main routes of toxicant introduction into the body is through oral ingestion and subsequent absorption from the gastrointestinal (GI) system, which represents first pass metabolism. Therefore, a critical component to the μCCA was the inclusion of the GI system mimic (Figure 2). We have developed a GI module that incorporates a mixture of cell types to better mimic realistic intestinal cell populations, which include absorptive enterocytes and mucus producing goblet-like cells [9-11]. The mixture of cells is cultured on a microporous membrane to allow introduction of the analyte of interest at the apical side, but limits passage to the basolateral side to only those analytes that successfully pass through the functional GI cell barrier layer (Figure 2C). For total system recirculation, a peristaltic pump is used with tubing connecting the analyte source and the apical GI surface (for continuous "ingestion"), and the basolateral GI surface is connected to the μCCA body chip (Figure 2A and 2B). Devices such as these are valuable not only as tools for toxicity screening but also as tools for screening drug candidates, indicating drug efficacies and side effects as well as combinatorial effects from mixtures of compounds, thus lessening the dependence on animal models.

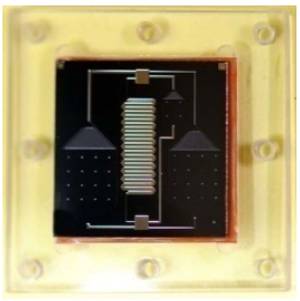

Figure 1. Micro-CCA device with fabricated organ chambers. Image provided by M. Shuler.

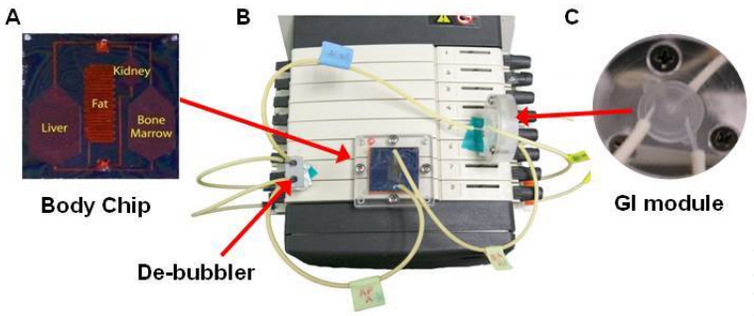

Figure 2. (A) Image of the systemic μCCA. Organ chambers and channels are fabricated to accurately scale the chamber size and the interconnecting channels so they are representative of *in vivo* circulating conditions for those organs. The other tissues of the body were represented by the external de-bubbler, which was a 200 μL reservoir. (B) Image of the systemic and GI tract μCCA experimental set-up. (C) The GI module housed in a plexiglass chamber with cells seeded on a semiporous membrane. Images provided by M. Shuler.

2. Electrochemical detection methods for cellular stress biomarkers

One type of cellular response to a toxicant is through the generation of extracellular biomarkers. In this manner, we can transform a toxicity response to a contaminant suite into a biomarker concentration. The main focus of our collaboration with Dr. Scott Banta at Columbia University is the generation of a streamlined platform for the rapid development of new biosensors that can be used to detect virtually any desired protein biomarker target. The overall selectivity and sensitivity of the biosensor are dependent not only on the recognition element, but also on the transducer used to detect the response. Therefore, our research combines generation of novel biorecognition elements with electrochemical transduction to fabricate powerful selective sensing modalities [12].

The process we have developed includes: biomarker (target) selection and immobilization, phage display to select binding peptides, peptide synthesis with a terminal thiol, quartz crystal microbalance (QCM) for *in-situ* monitoring of peptide immobilization, and analyte detection using electrochemical techniques (Figure 3A). Target selection involves several rounds of M13 phage display followed by enrichment of short unstructured peptides that bind to the desired target with increased affinity. For the sensor performance, the selected, final round peptides are chemically synthesized and immobilized on a gold surface, allowing for detection of the target using QCM (Figure 3B) or electrochemical impedance spectroscopy (EIS) (Figure 3C). The use of short unstructured peptides over more complex protein-based affinity scaffolds has several advantages: 1) peptides are stable and resistant to harsh environments, 2) peptides can be synthesized easily and inexpensively, and 3) peptides can be more amenable than antibodies to engineering at the molecular level due to their smaller size. In addition, peptide immobilization on gold electrodes has been well established.

We demonstrated the utility of this approach by creating a novel peptide-based electrochemical biosensor for the enzymes alanine transaminase (ALT), a well known biomarker of

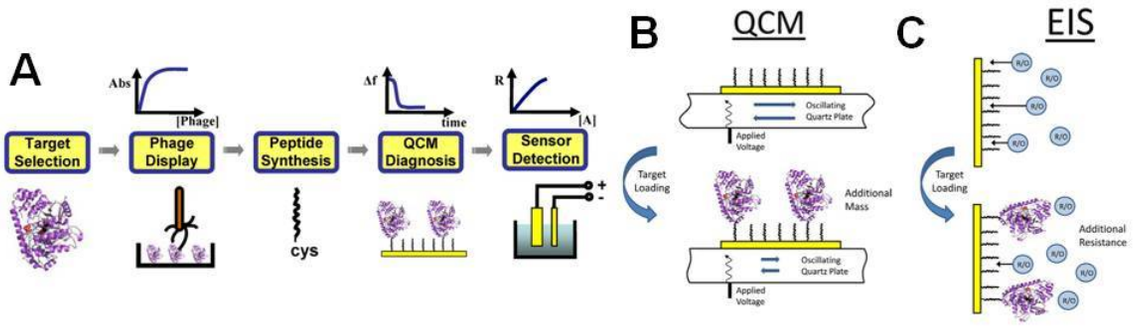

Figure 3. Schematic diagram illustrating the general process of biosensor development. (A) Work flow diagram for biosensor development: 1. Target protein biomarker selection, 2. Phage display selection, 3. Peptide synthesis, 4. QCM diagnosis, 5. Biomarker detection. B) The basic principle of QCM where the binding of the target protein to the immobilized peptides causes a frequency change in the oscillation of the quartz crystal. C) The basic principle of EIS where the binding of the target protein to the immobilized peptides causes increased resistance to the reaction of an added redox couple.

hepatotoxicity. The sensor was prepared using the selected ALT peptide that had been modified with a C-terminal cysteine to facilitate the immobilization on a gold surface. Once the peptide had been immobilized, any remaining bare gold was blocked by the addition of free cysteine to prevent non-specific binding of the target directly to the gold surface. The binding and blocking processes were monitored by QCM, cyclic voltammetry (CV) and EIS. The peptide immobilization resulted in a frequency drop in the QCM signal due to the increased mass loading, a drop in current was detectable by CV, and an impedance increase in the EIS due to the blocking of the gold surface. The packing density of the surface-bound peptide can be calculated using the Sauerbrey equation [13]:

$$\Delta f_m = -C_f x\ \Delta m \tag{1}$$

where Δf_m is the frequency change due to mass loading, Δm is the mass change at the QCM crystal surface and $C_f = 0.0566$ Hz/(ng/cm^2) for a 5 MHz AT-cut crystal at 20°C. The frequency drop of the QCM due to the immobilization of the peptide was roughly 21 Hz, which correlates to a packing density of $2x10^{-10}$ mol/cm^2 or $1.2x10^{14}$ molecule/cm^2 using a peptide molecular weight of 1851 g/mol.

Next QCM, CV and EIS were used to demonstrate the affinity and specificity of the immobilized peptide for ALT (Figures 4 and 5). A frequency drop (Df = -31 Hz) in QCM was observed upon binding of ALT versus the frequency of the sensor in buffer alone (Figure 4A). A current decrease in CV (Figure 4B) as well as a large impedance increase (Figure 4C) was measured upon addition of ALT, while buffer alone resulted in no change.

Figure 5 shows the specificity of the peptide (Au-Peptide) for ALT over streptavidin (SA) or bovine serum albumin (BSA). The greatest frequency change of -31 Hz was observed with ALT. Although a small frequency change (about -3 Hz) was seen with SA and BSA, this change may be due to a small amount of non-specific binding of the proteins to unoccupied sites on the surface or non-specific interactions with the peptide itself.

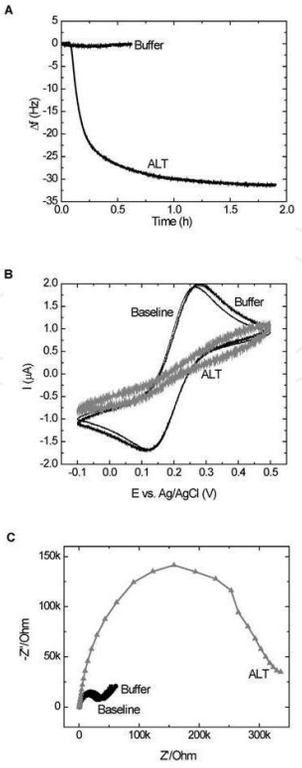

Figure 4. Sensor operation. A) QCM frequency change of Au-Peptide electrode in Buffer alone and in 10 mg/mL ALT, B) CV of Au-Peptide electrode before (Baseline) and after Buffer alone or ALT binding, C) EIS of Au-Peptide before (Baseline) and after Buffer alone or ALT binding. After incubation in Buffer or 10 mg/mL ALT, the electrodes were transferred to 1 mM solution of $Fe(CN)_6^{4-/3-}$ in 0.1 M $NaClO_4$ for the EIS measurements.

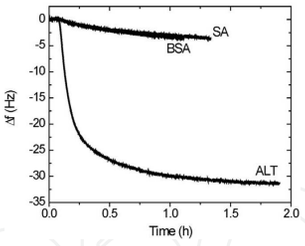

Figure 5. Specificity of the ALT biosensor. The shift in QCM frequency in response to injections of SA, BSA or ALT on the Au-Peptide modified crystal. The concentrations of all three solutions were 10 μg/mL.

For quantitative measurements, CV was not performed due to the limited detection range since the current decreases upon target binding. Therefore, we performed only QCM and EIS using a range of ALT concentrations (Figure 6). A quantitative response was observed for both QCM (Figure 6A) and EIS (Figure 6B) for the range of ALT concentrations tested. The LOD obtained by QCM is 60 ng/mL, while EIS has a LOD of 92 ng/mL. The sensitivity of the QCM system was 8.9 +/- 0.9 Hz/(mg/mL), while the sensitivity of the EIS system was 142 +/- 12 impedance percentage change %/(mg/mL). The quantitative response achieved for both QCM and EIS validates that both methods could be used as a sensing technique in quantitative ALT measurements.

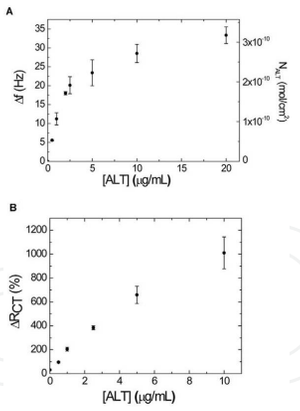

Figure 6. Response curves of ALT binding. Measurements were made using QCM (shown as absolute value of frequency change) (A) and EIS (B). Each run was performed using a single electrode with successive tests in ALT solutions from low to high concentration. The apparent amount of bound ALT (N_{ALT}) for the QCM measurements was calculated using Eqn. 1 and is shown on the right ordinate. Error bars represent standard deviations obtained from triplicate measurements.

In addition to the generation of this ALT-specific recognition element, we have developed a recognition element for the cardiac specific biomarker, troponin I (TnI) [13, 14]. Again, phage display was employed to generate the recognition peptide while QCM and EIS validated and quantified the binding events and specificity of the peptide for the target, TnI. Therefore, the generation of a peptide recognition element specific for the binding of either ALT or TnI followed by immobilization onto a gold surface for signal transduction supports this method of biorecognition element generation for the detection of any specific cellular stress biomarker. The recognition peptide provides the next step toward increasing stability over antibodies, but quantitative impact versus longevity depends upon how it is used in a more mature device. We are currently engaged in transitioning the peptide recognition schemes onto a fieldable chip. Reuse conditions for the chip must also be investigated but likely involves introduction of a release buffer with glycine-HCl.

We recognize that gold components within microfluidic devices, specifically as electrode materials, are prone to biofouling. In an effort to use an electrode material both more resistant to biofouling and possessing a larger potential range compared to noble metal electrodes [15-17], we developed a new method for the fabrication of carbon paste electrodes (CPEs) that optimizes their stability in a flow-based microfluidic device [18]. The greater stability of these CPEs results from exploiting beneficial properties of both soft and rigid composites, which are used as the binder, during CPE fabrication. As a result of our collaboration with Dr. Charles Henry at Colorado State University, we have developed a mixed binder to create on-chip CPEs for flow-based devices. The mixed binder composed of a soft composite (mineral oil) and a rigid composite (poly(dimethylsiloxane) (PDMS)) enhanced the overall CPE robustness and electrochemistry over that of a CPE fabricated with mineral oil or PDMS alone. Analysis of the CPE performance was carried out using cyclic voltammetry in static solutions or amperometry with flow injection analysis.

The CPEs are fabricated simply by filling channels molded in previously cross-linked PDMS using a method analogous to screen printing with the CPE mixture, which is composed of

graphite powder and the PDMS:mineral oil binder (Figure 7). Further, we demonstrated that the PDMS: mineral oil CPEs can easily be chemically modified for the detection of biologically relevant molecules. The monitoring of thiols provides an indication of the functioning of numerous critical cellular pathways [19, 20]. Traditional carbon paste electrodes can be used to detect thiols, however, they suffer from low peak currents due to poor interactions between the carbon and the thiols. Therefore, we added the electrocatalytic reagent cobalt phthalocyanine (CoPC), which is widely used as a reduction/oxidation mediator for lowering the overpotential of thiols [21-23], to decrease decrease the detection potential and increase the peak current obtainable with carbon electrodes. The model analyte dithiothreitol (DTT) was used to demonstrate the sensitivity of the CoPC modified CPEs for the detection of thiols. Cyclic voltammetry and amperometry were used to compare the CoPC modified CPEs to bare CPEs (Figure 8). The detectable electrocatalytic process occurs in two steps that involve the initial electrochemical oxidation of Co(II)phthalocyanine followed by the chemical oxidation of DTT as it regenerates the Co(II)phthalocyanine [23]. Figure 8A shows the cyclic voltammograms of a CoPC modified CPE (solid line) versus an unmodified CPE (dashed line) of 1 mM DTT in MES buffer (2-(*N*-morpholino)ethanesulfonic acid, 30 mM, pH 7.4). Under these conditions, the unmodified CPE failed to detect the DTT whereas the expected oxidation peak of DTT was observed for the CoPC modified CPE [24]. We evaluated the performance of the CPEs for DTT detection with respect to the amount of CoPC added to the graphite and determined that a mixture of 12% CoPC in graphite performed the best (data not shown). Also, the composition of the binder was investigated to identify the best DTT detection performance, and the ratio of 2:3 PDMS:mineral oil was optimal to maintain robustness and electrochemical performance. The secondary means to characterize the performance of the CoPC modified CPEs involved flow injection analysis using amperometric detection for the continuous detection of DTT (Figure 8B). Using a CoPC modified electrode, we observed nearly a 2-fold improvement in the electrochemical signal (4.0 ± 0.2 nA (n = 3) versus 2.5 ± 0.2 nA (n = 3)) for a bare CPE for 100 μM DTT. Additionally, the limit of detection (LOD, defined as the concentration yielding a 3x larger signal than baseline noise) for DTT with a CoPC modified CPE was 2.5 ± 0.2 μM (n = 5) versus 16.8 μM (n = 5) for an unmodified CPE.

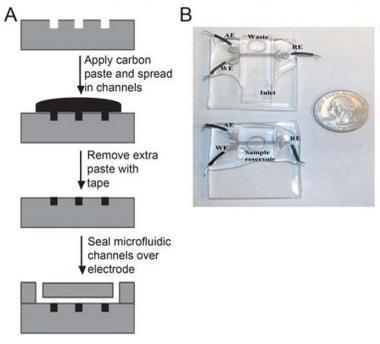

Figure 7. Flow-based microfluidic system using CPEs. (A) Schematic for electrode fabrication process (side view), (B) Photograph of electrode alignment in a microfluidic device for the flow injection system with amperometric detection (top) and for cyclic voltammetry study (bottom). Size of electrodes: 250 μm wide and 50 μm deep. Electrode spacing (center-to-center), 300 μm. Microfluidic channel dimension: 250 μm wide, 50 μm deep and 2.5 cm long. Reproduced by permission of The Royal Society of Chemistry.

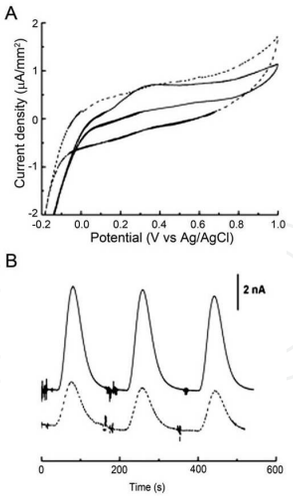

Figure 8. Comparison of working electrode performance for DTT detection between CoPC modified CPE (solid line) and unmodified CPE (dashed line). (A) Cyclic voltammograms of 1 mM DTT in 30 mM MES buffer, pH 7. (B) Flow injection analysis with amperometric detection of 100 μM DTT using 30 mM MES, pH 7, as a running buffer. Paste composition ratio is 5 : 3 : 2 (graphite:oil:PDMS). Off-chip reference and auxiliary electrodes were used. Applied potential: 0.2 V (vs. Ag/AgCl (3 M KCl)) for both types of working electrodes with Pt wire as an auxiliary electrode. Flow rate: 60 mL min^{-1}. Reproduced by permission of The Royal Society of Chemistry.

Next, we chemically modified the CPEs with multi-walled carbon nanotubes (MWCNT) for the detection of catecholamines. The importance of the ability to detect biologically relevant compounds from cells is critical not only for our current application of detection of toxic compounds in the environment, but also for the detection or monitoring of debilitating diseases. Catecholamines like dopamine are known to be involved in the progression of neurological diseases such as Parkinson's and Alzheimer's [25, 26]. Using the MWCNT modified CPEs, we were able to detect the release of dopamine from cultured rat PC12 cells. The data for the flow injection analysis for the detection of 10 μM dopamine is shown in Figure 9 using both MWCNT modified (solid line) and unmodified (dashed line) CPEs. A more significant improvement in signal was observed for the MWCNT modified CPEs when detecting catecholamines, namely dopamine, than shown above for DTT. We determined that the lowest dopamine concentration detectable by MWCNT modified CPEs was 50 nM whereas concentrations below 500 nM for unmodified CPEs were undetectable. This order of magnitude increase in detection likely results from the increased surface area of the electrode achieved with the addition of the MWCNTs and therefore, the peak currents obtained for the CPEs.

We also observed the release of catecholamines from PC12 cells upon exposure to high concentrations of potassium. At each time point, the catecholamine released was measured from potassium-stimulated PC12 cells (6×10^4 cells/time point) using the flow injection analysis system with MWCNT modified CPEs. Figure 10 shows the plot of the peak area versus time for the duration of potassium exposure. At three minutes, the calculated concentration of released catecholamine was estimated to be 3.6 μM (58.3 pM/cell). Concentrations of catecholamine released by PC12 cells upon exocytotic events have been reported to be 67 μM [27, 28] or 20-160 μM dopamine from 1.3×10^4 cells exposed to calcium stimulation [29]. The lower levels of catecholamines detected by our system may be the result of very low capture efficiency

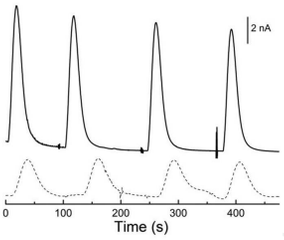

Figure 9. Flow injection analysis of dopamine. Comparison of unmodified CPE (dashed line) and MWCNT modified CPE (solid line). Sequential injections of 10 μM dopamine. Off-chip reference and auxiliary electrodes were used. Applied potential: 0.6 V (vs. Ag/AgCl (3M KCl)) with Pt wire as an auxiliary electrode. Flow rate: 60 mL min^{-1}. Reproduced by permission of The Royal Society of Chemistry.

of this non-optimized CPE design. Interestingly, it is likely that neuronal cells, like PC12s, have a process to re-uptake catecholamines, and this common theory is supported by the sharp decrease in catecholamine signal we observed with our MWCNT modified CPE system at time points after the significant release that occurs at three minutes.

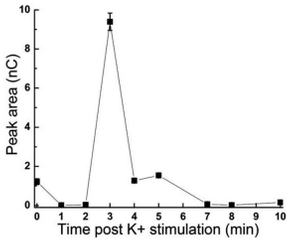

Figure 10. Effect of potassium on catecholamine release from PC12 cells. 6.15 x 10^4 cells were stimulated at each time point. Supernatant was removed and stored on ice until analysis. All experimental conditions same as in Fig. 9. Reproduced by permission of The Royal Society of Chemistry.

The ability to determine the biological consequences of known and unknown toxicants is essential for the protection of the environment and soldier health. We have generated a novel approach for the development of carbon paste electrodes that are integrated, robust, and low cost for microfluidic detection of extracellular biomarkers [18]. Figs 8B and 9 show that the CPEs are stable and reusable over many cycles, although the exact number of cycles depends upon the sample matrix and the run conditions. The CPEs can be readily modified to monitor biologically informative species, which can indicate the cellular responses to environmental stimuli. With its simple modification scheme to introduce electrode selectivity and its intricate design capability allowing for detailed electrode features, this biosensing system can be easily incorporated into many detection platforms.

3. Cell-based sensor designs

We have developed a simple and direct *in vitro* method to control the alignment and elongation of cells in order to form self-organized 3D tissues as part of a collaborative effort with Dr. Ali

http://dx.doi.org/10.5772/52438

Khademhosseini's laboratory at Harvard University. By harnessing the intrinsic potential of certain cells to form aligned tissues *in vivo*, we can generate functional tissues *in vitro* by confining the cells in the appropriate 3D microarchitecture [30]. Cells possessing the prerequisite ability to self-organize *in vivo* include fibroblasts, myoblasts, endothelial cells, and cardiac stem cells. The process involves embedding the cells in microengineered 3D gelatin methacrylate (GelMA) hydrogels, which are micropatterned into high aspect ratio rectangular constructs. In contrast, the cellular alignment in unpatterned microconstructs remained random. By precisely controlling this microgeometry, we can induce the controlled cellular alignment and elongation throughout the entire engineered construct in a user-defined manner. We envision this technology to enable the construction of engineered functional 3D tissues with aligned cells and anisotropic function. Additionally, we extended this technology for the development of a cell-based biosensor for the detection of cardiotoxicity in real-time by following changes in cardiomyocyte beating properties [31].

To demonstrate the control of cellular alignment and elongation properties *in vitro*, we encapsulated 3T3-fibroblasts (10 x 10^6 cell/mL) in a GelMA construct (800 μm (l) x 150 μm (h) x 50 μm (w)). A 1 mm border surrounded the multiple parallel microconstructs to serve as an unpatterned control (Figure 11). The GelMA macromer concentration (5% w/v, ~80% methacrylation degree) was chosen to maintain the mechanical stiffness but still preserve cell viability and allow the micropatterning of the intricate cell-laden features. After 1 day, elongation of the cells was observed mainly along the edges of the micropatterns and followed the major axis of the channel, but spread throughout the construct by 4-5 days. The lower series of panels illustrates the lack of alignment within the unstructured GelMA. Additionally, the elongation and alignment responses could be controlled by the cell density, hydrogel concentration, and culture time (data not shown) further demonstrating the ability to fine tune these cellular properties.

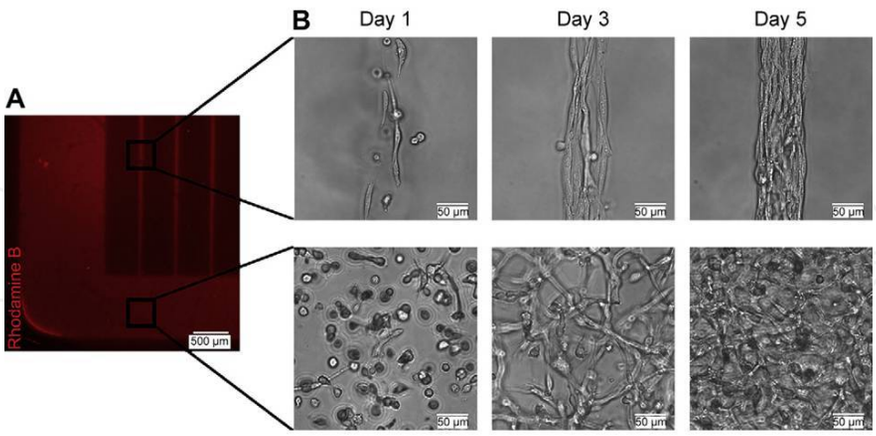

Figure 11. Cell morphology and organization as a function of time in patterned and unpatterned microconstructs. Patterning 3T3-fibroblast-laden 5% GelMA hydrogels into high aspect ratio rectangular microconstructs (50 μm (w) x 800 μm (l) x 150 μm (h)) induced cellular alignment and elongation, while cellular orientation in unpatterned hydrogels remained random. (A) Rhodamine B stained GelMA hydrogel construct shows patterned and unpatterned regions. (B) Representative phase contrast images of 3T3-fibroblasts (10 x 10^6 cells/mL) encapsulated in patterned (top row) and unpatterned regions of the GelMA hydrogel (bottom row) on days 1, 3 and 5 of culture show that elongation increases over time for all hydrogels, while alignment is only induced in patterned constructs.

We quantitatively analyzed the effects of microgeometry by patterning cells in GelMA constructs with a standard length and height but varying widths (800 μm (l) x 150 μm (h) x 200, 100 or 50 μm (w)) (Figure 12). We observed a strong correlation between the ability of cells to align and elongate throughout the construct with the decrease in width. Alignment was assessed by counting cells whose nuclei were within 10° of the preferred nuclear orientation as described [32]. Overall nuclear alignment and shape index were evaluated with NIH ImageJ software to evaluate cell alignment and elongation [33, 34]. The narrowest microconstruct had the best alignment with 64 ±8% of cells aligned (Figure 12A), and this increased to ~90% if the preferred nuclear orientation was defined to within 20° (Figure 12F). That alignment percentage decreased with increased channel width resulting in 40 ±6% for the 100 μm and 31 ±8% for the 200 μm channels. However, compared to the unpatterned control, the 100 μm channel was still statistically different ($p < 0.01$). The 200 μm channel was not statistically different and the unpatterned control showed only 19 ±9% alignment to the construct (Figure 12A). In comparing the nuclear shape index (Figure 12B), the results were consistent with the lowest mean nuclear shape index corresponding to the 50 μm wide rectangular microconstructs (0.807 ±0.02). The 100 μm and 200 μm wide micropatterns displayed 0.869 ±0.03 and 0.917 ±0.02 mean nuclear shape indices, respectively, while the unpatterned control had a mean nuclear shape index of 0.923 ±0.03 (Figure 12B). Figures 12G-J show representative images of the unpatterned and patterned microconstructs where increasing cell alignment and elongation is visible in constructs of decreasing width.

Next, we expanded the number of cell types used for micropatterning to include additional, self-organizing cells (human umbilical vein endothelial cells (HUVEC), rodent myoblasts (C2C12), and rodent cardiac side population cells (CSP)) and non-organizing cells (Hep-G2) to investigate the applicability of this technique to engineer a variety of tissues representative of vascular system, skeletal muscle, and myocardial tissues, respectively (Figure 13). Accurately mimicking the *in vivo* microarchitecture of these systems would require highly elongated, organized and aligned cell-ECM constructs. As a control, we selected a cell type that lacks the intrinsic potential for self alignment *in vivo* or *in vitro*, human liver carcinoma cells (Hep-G2). All cells were encapsulated in 5% (w/v) GelMA and micropatterned in 50 μm wide rectangular microconstructs. After a five day culture time, the patterned and unpatterned cells were stained with DAPI and phalloidin to visualize cell nuclei and F-actin, respectively (Figure 13A and B). Images revealed the HUVEC, C2C12, and CSP cells to be highly aligned, elongated, and interconnected along the major axis of the micropatterned hydrogels. In contrast, the unpatterned cells remained random with minimal nuclear organization observed only at the edges of the hydrogel. Significant differences were observed upon quantitative analysis for both cellular alignment and elongation (Figure 13C) as well as for mean nuclear shape index (Figure 13D) for the HUVEC, C2C12 and CSP cells when comparing the patterned to unpatterned constructs. Consistent with the lack of intrinsic potential, Hep-G2 cells did not show a significant difference in observed alignment and elongation between the patterned and unpatterned hydrogel constructs, but rather formed cell clusters of multiple cell nuclei regardless of the aspect ratio of the microconstructs. Therefore, the *in vivo* ability of cells to form aligned tissues is required to promote this alignment and elongation behavior *in vitro* via specified microgeometry.

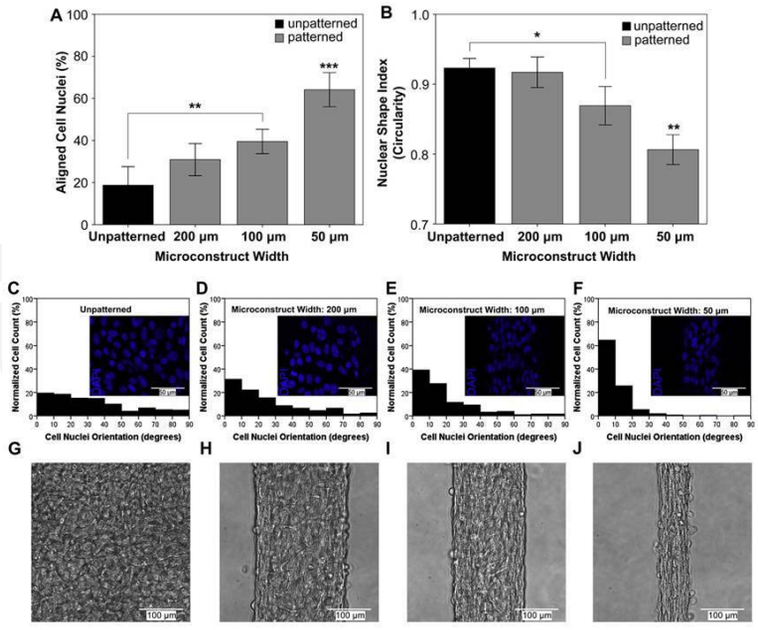

Figure 12. Cell elongation and alignment as a function of microconstruct width. Decreasing the width of patterned rectangular 5% GelMA microstructures (800 µm (l) x 150 µm (h)) increased 3T3-fibroblast alignment as well as nuclear elongation after 5 days of culture. (A) Mean percentage of aligned cell nuclei (within 10° of preferred nuclear orientation) shows 100 µm constructs were significantly more aligned than unpatterned controls, while 50 µm constructs were significantly more aligned than all other groups. (B) Mean nuclear shape index (circularity = 4*π*area/perimeter^2) shows a similar pattern with 100 µm constructs having a significantly lower index than unpatterned controls, while 50 µm constructs were significantly different than all other groups. (C), (D), (E) and (F) Histograms of the relative alignment in 10° increments demonstrates increased cellular alignment with decreased microconstruct width. (G), (H), (I) and (J) Representative phase contrast images of unpatterned, 200 µm, 100 µm and 50 µm wide microconstructs, respectively, show significantly increased cell alignment and elongation inside the constructs with decreasing width. (Error bars: ± SD; ***$p < 0.001$; **$p < 0.01$; *$p < 0.01$).

In the quest to form a 3D tissue construct, we tested the ability of the self-assembly properties of the microconstructs by generating a closely spaced rectangular array of cell-laden GelMA hydrogels (Figure 14). We again used 3T3-fibroblasts embedded in 5% (w/v) GelMA patterned into 50 µm wide microconstructs that were spaced 200 µm apart. After four days, the microconstructs had merged in some sections along the channel (Figure 14A, red arrows). The merging continued until day seven when the constructs had completely converged into a larger macroscale tissue construct (~ 1cm^2) (Figure 14B). F-actin staining of the macroscale tissue revealed a fiber network that was aligned in one direction along the major axis of the micropatterns and extended across the voids between the micropillars once the constructs fully converged (Figure 14C).

Since a major goal of this research program is the development of portable devices that can monitor toxicity, we applied the ability to form a 3D microengineered hydrogel for the development of a cell-based biosensor capable of detecting cardiotoxicity using lens-free imaging [31]. We have developed a cell-based biosensor that utilizes cardiomyocytes that are imaged using a lens-free imaging technique with a complementary metal oxide semi-conductor (CMOS) imaging module extracted from a standard webcam. The cardiomyocytes are derived from mouse embryonic stem cells (ESCs) and tested for the changes in beating rates

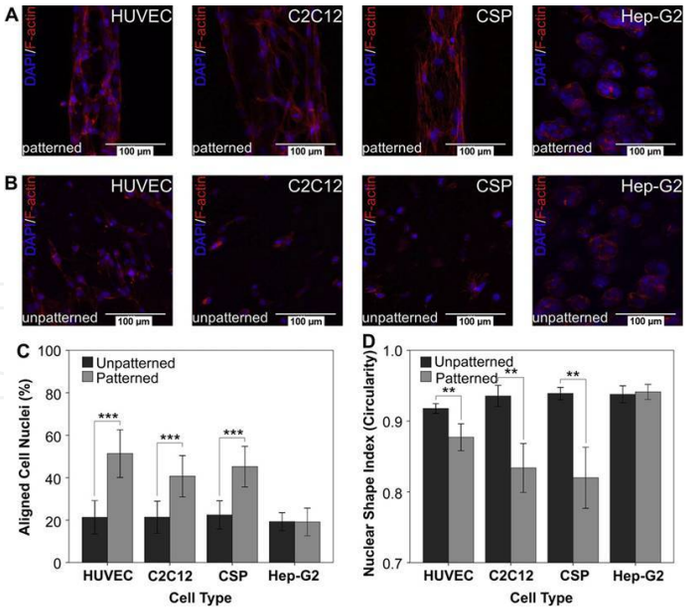

Figure 13. Cell elongation and alignment in multiple cell types. Patterning cell-laden 5% GelMA hydrogels into rectangular microconstructs (50 µm (w) x 800 µm (l) x 150 µm (h)) induced cellular alignment and elongation after 5 days of culture only in cell types possessing an intrinsic potential to organize into aligned tissues in vivo, while cellular orientation in unpatterned parts of the same hydrogels remained random. Representative z-stack overlays of DAPI/F-actin staining of (A) patterned and (B) unpatterned hydrogels laden with HUVEC, C2C12, CSP, and Hep-G2 cells respectively show patterning induced aligned and elongated cell-network formations in HUVEC, C2C12 and CSP cells and patterning independent cell-cluster formations in Hep-G2 cells. (C) Mean % of aligned cell nuclei (within 10° of preferred orientation) shows patterned HUVEC-, C2C12- and CSP-laden constructs were significantly more aligned than unpatterned controls, while in Hep-G2-laden constructs patterning failed to induce cell alignment. (D) Mean nuclear shape index (circularity = $4*\pi*area/perimeter^2$) similarly shows patterned HUVEC-, C2C12- and CSP-laden constructs were significantly more elongated than unpatterned controls, while in Hep-G2-laden constructs patterning failed to induce cell elongation. (Error bars: ± SD; $^{**}p < 0.01$; $^{***}p < 0.001$)

and beat-to-beat variations upon exposure to known cardiotoxic compounds, isoprenaline and doxorubicin. Figure 15 shows a schematic of the experimental setup with the CMOS module positioned below the cardiomyocytes cultured in a commercially available chamber slide while the white LED light source, controlled by a pinhole, is positioned over the cell culture. The beating responses are monitored in real-time via an imaging processing program. Initial characterization of the lens-free system prior to exposing the cardiomyocytes to any drugs involved the cells being cultured in standard medium and the beating rates monitored continually for 150 minutes (Figure 16). An average of 100 beats per minute was observed and was consistent with literature reports [35, 36]. Only a 3% variation was measured in the beating rates and indicated the cells displayed normal beating patterns.

In order to measure the chronotropic effects of a drug on our cardiomyocytes-based biosensor, we selected two drugs with opposing effects: isoprenaline is a sympathomimetic β-adrenergic agonist drug that can cause an abnormally increased heart rate (tachycardia) and doxorubicin is an anti-cancer drug with side effects that can lead to an abnormally decreased heart rate (bradycardia). In the case of isoprenaline, different concentrations (1, 5, 10, and 100 nM) were dissolved in culture medium and added to the chamber slide. Measurements were collected consecutively for 20s over a period of 1 min. Figure 17A shows the increases in relative beating

http://dx.doi.org/10.5772/52438

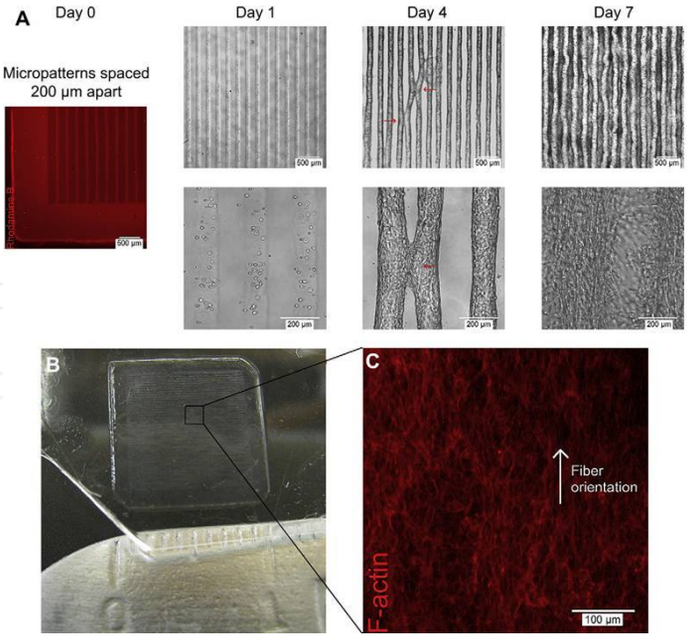

Figure 14. Self-assembly of multiple aligned microconstructs into a macroscale and aligned 3D tissue construct. 3T3-fibroblast-laden 5% GelMA hydrogels patterned into rectangular microconstructs (50 µm (w) x 800 µm (l) x 150 µm (h)) spaced 200 µm apart self-assembled into macroscale and aligned 3D tissue constructs after 7 days of culture through convergence of multiple, aligned microconstructs. (A) Rhodamine B stained hydrogel shows initial microconstruct spacing of 200 µm at day 0; representative phase contrast images of cell-laden microconstructs at days 1, 4 and 7, respectively, show focal points of contact between neighboring aligned microconstructs at day 4 (red arrows) and formation of a macroscale 3D tissue construct at day 7. (B) Image of a 1 cm x 1 cm, self-assembled 3D tissue construct at day 7. (C) Representative F-Actin staining of the middle xy-plane of a macroscale 3D tissue construct shows oriented actin fiber organization in a single direction.

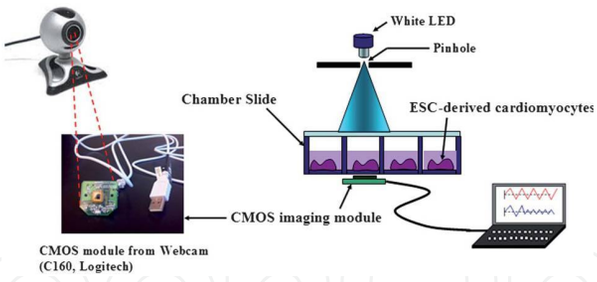

Figure 15. Schematic of the experimental setup. ESC-derived cardiomyocytes were plated on a chamber slide. The white LED and pinhole combination was used as a light source for imaging the beating cardiomyocytes. The real-time beating rates of the cardiomyocytes were measured using the CMOS imaging module which was controlled by an image processing program. Reproduced by permission of The Royal Society of Chemistry.

rates corresponding to the increase in isoprenaline concentration. After introduction of the isoprenaline, the time interval between the beats became shorter and a new pulse pattern was observed that indicated an increase in the beating rate (Figure 17B). Following a 12 min exposure, the beating rates as a function of isoprenaline concentration were compared (Figure 17C). The beating rates increased 24% and 44% for 1 and 5 nM isoprenaline, respectively, and 70% for both 10 and 100 nM. This resulted in a statistical difference between 1, 5 and 10 nM, but not between 10 and 100 nM. The patterns we observed are consistent with reported studies.

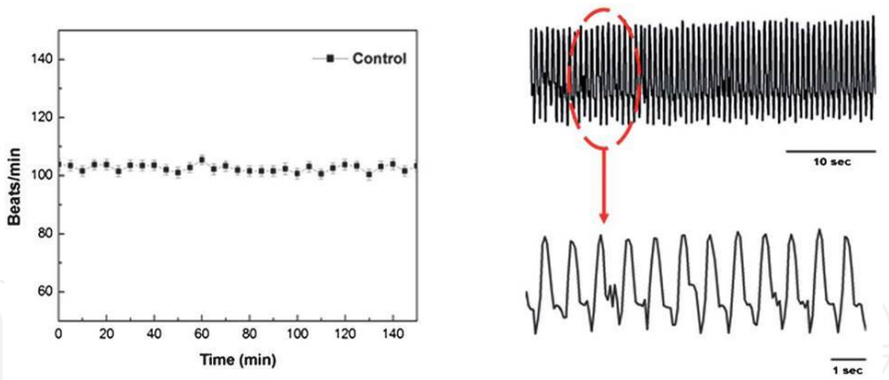

Figure 16. Characterization of the lensfree cardiotoxicity detector. Prior to injection of the drugs, the ESC-derived cardiomyocytes were cultured in normal medium and their beating rates were observed for 150 min. The beating rates were stable and the beating signal had a regular pulse pattern. Reproduced by permission of The Royal Society of Chemistry.

[36, 37]. An increasing isoprenaline concentration resulted in an increase in the beat-to-beat variation (Figure 17D).

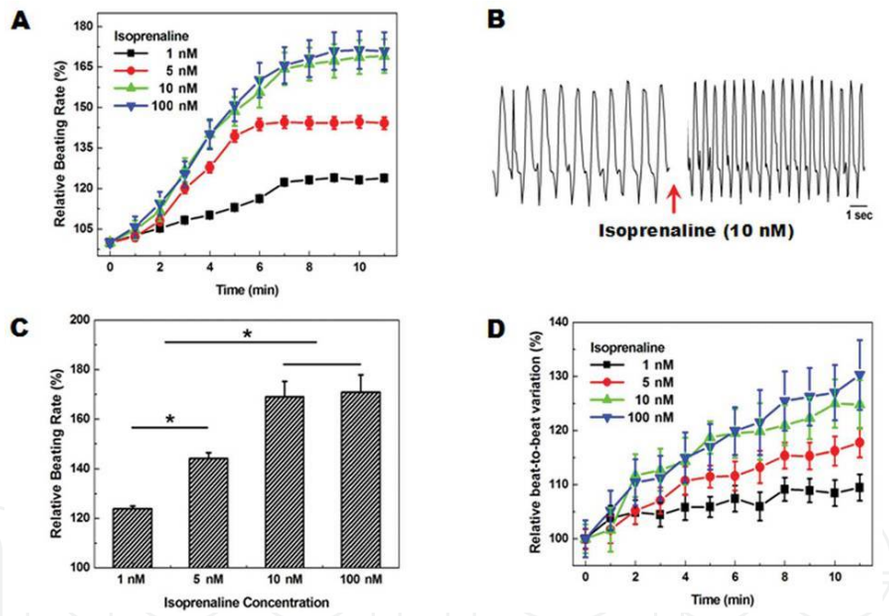

Figure 17. Chronotropic effects of cardiomyocytes under treatment of different concentrations of isoprenaline (1, 5, 10 and 100 nM). (A) The change in beating rate. The beating rates increased after isoprenaline injection. (B) A plot of the image difference value. A pulse pattern was observed. The decreased beating intervals were observed clearly after isoprenaline was injected. (C) The change in beating rates over time during the first 12 min after treatment of isoprenaline. (D) The beat-to-beat variations. Beat-to-beat variations increased under treatment of isoprenaline. * shows a significant difference in variance ($p < 0.05$). For statistical analysis, one-way ANOVA was used. Reproduced by permission of The Royal Society of Chemistry.

As expected for doxorubicin, exposure to the drug slowed beating rates in a time dependent manner (Figure 18A). Again, the drug was dissolved in culture medium at various concentrations (10, 100, 200 and 300 μM) and added to the chamber slide. The measurements were

http://dx.doi.org/10.5772/52438

collected consecutively for 30s for a period of 5 min. The higher concentrations (200 and 300 μM) of doxorubicin resulted in a rapid decrease in the beating rate, and the beating stopped after 20 min for the highest concentration. The effects were much slower for the lower concentrations, however, a decrease in beating rate was still observed. The pulse pattern slowed as the interval between the spikes became longer (Figure 18B) indicating a decrease in the beating rates. A change in amplitude was also apparent, however, our imaging processing program did not contain an amplitude detection algorithm, and the apparent decrease could be contributed to a small difference between the reference and the live frame images. At 100 min, the beat rates as a function of doxorubicin concentration were compared and are shown in Figure 18C. A statistical difference was observed at 100 and 200 μM doxorubicin with the beating rates decreasing 26% and 54%, respectively. We also measured the beat-to-beat variations induced by the different doxorubicin concentrations (Figure 18D). The response time of the beat-to-beat variations was slower than observed for the change in beating rates. These findings are consistent with electrical measurements from a previous study [38]. Following injection of the doxorubicin, the beating of the ESC-derived cardiomyocytes became more irregular than was observed in the presence of isoprenaline.

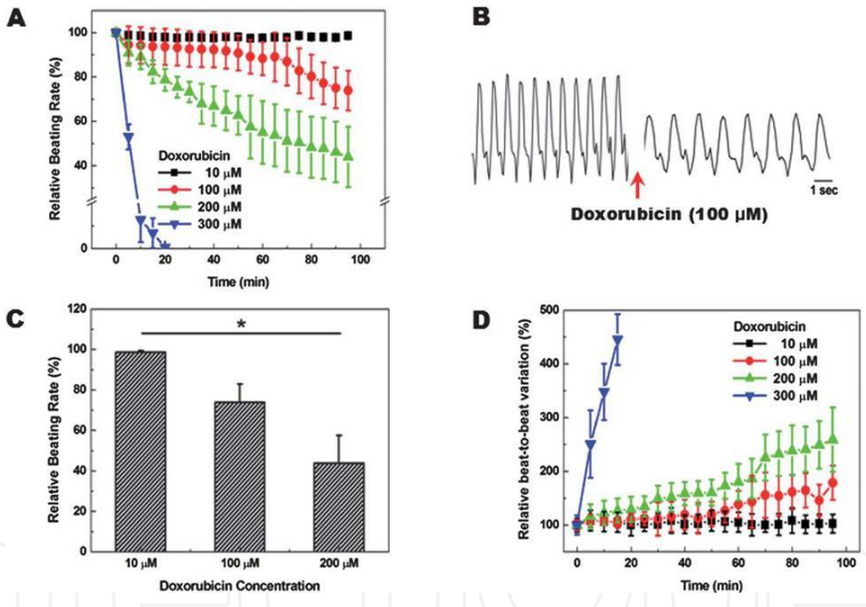

Figure 18. Chronotropic effects of cardiomyocytes under treatment with doxorubicin (10, 100, 200 and 300 μM). (A) The change in beating rate. The beating rates decreased after doxorubicin injection. (B) The beating signal. The increased beating intervals were clearly observed after doxorubicin injection. (C) The change in beating rates at 100 min after the treatment with doxorubicin. (D) The beat-to-beat variations. In contrast to beating rates, the beat-to-beat variations increased after treatment with doxorubicin. * shows a significant difference in variance ($p < 0.05$). For statistical analysis, one-way ANOVA was used. Reproduced by permission of The Royal Society of Chemistry.

The development of a cell-based biosensor using an off-the-shelf CMOS system represents a low-cost, relatively straight forward system that can be useful in monitoring the physiological response of cells to a drug or contaminant. We envision the expansion of this platform to harbor complex matrices of cells that recapitulate major organ systems and respond to toxicity via different modes of action.

Our collaborative efforts with Dr. Robert Langer at the Massachusetts Institute of Technology have yielded the development of sacrificial melt-spun interconnected microfibers as an artificial vascular system [39, 40]. The system is based on the initial experiments by Bellan, *et al.* that used standard sugar-based cotton candy to create an interconnected 3D microchannel network inside several materials, including polydimethylsiloxane (PDMS), epoxy, and polycaprolactone (PCL) [39]. Briefly, the microchannel network of cotton candy (attached to larger sticks of sugar in order to produce macrochannel interfaces) was embedded within the material of choice, which was then allowed to solidify. The embedded sugar fibers were dissolved by submerging the structure in a warm water bath, leaving behind a 3D microchannel network in the shape of the cotton candy. The resulting device supported flow of a solution of either 2 μm polystyrene spheres or heparinized whole rat blood. The channel sizes and spacing between channels were very similar to the relevant parameters for natural capillary beds thus providing an excellent means to replicate the cardiovascular network.

We next evolved the microvasculature network into a more complex 3D structure with the integration of larger, lithographically patterned microchannels [40]. This 3D structure is composed of a melt-spun sugar microfiber network "sandwiched" between a top and bottom lithographically patterned microfluidic system, and the fabrication process is detailed in Figure 19. A comparison of the filling ability was made between our hybrid device and a device with the lithographically patterned channel system connected by simple, vertical pipes. Both were filled with a fluorescent dye solution to visualize the extent of delivery into the device volume (Figure 20). Fluorescent dye was carried only to localized regions within the device lacking the 3D microfluidic network (Figure 20B). However, fluorescence was observed throughout the device volume for the hybrid device containing the microfluidic network (Figures 20C, 20D, and 20E). This indicated that the microfluidic network was well distributed throughout the device and thus greatly increased the channel surface area. We achieved an approximate five-fold increase in total volume addressed with the inclusion of the microfluidic network between the larger, lithographically patterned channel systems. Consequently, with this increased surface area comes an order of magnitude increase in the measured flow resistance ranging from 12-27 psi min mL^{-1} compared to the device lacking the microfluidic network (~0.5 psi min mL^{-1}). The drastic difference can be explained by comparing the cross-sectional area of the smallest channels of the two devices. The conventional device contains channels with the smallest cross-section of 100 μm x 50 μm, while hybrid channels are much smaller at approximately 10 μm, which is similar to a natural capillary. We also observed some device-to-device variations in the flow patterns due to the differences in the volume of sacrificial material, the fiber density, and the interfaces between the fiber network and the larger lithographic pattern. Nevertheless, a hybrid device with a combination of conventional planar microfluidics and a 3D microchannel network may provide the best option to deliver the highest volume of nutrients and oxygen to an embedded cell population while maintaining the desired channel density and interconnectivity.

We envision a hybrid device such as this containing a capillary bed-like vasculature to be a valuable tool for tissue engineering applications involving cell embedded scaffolds or biomaterials as a means to exchange oxygen and nutrients, remove waste products, and

http://dx.doi.org/10.5772/52438

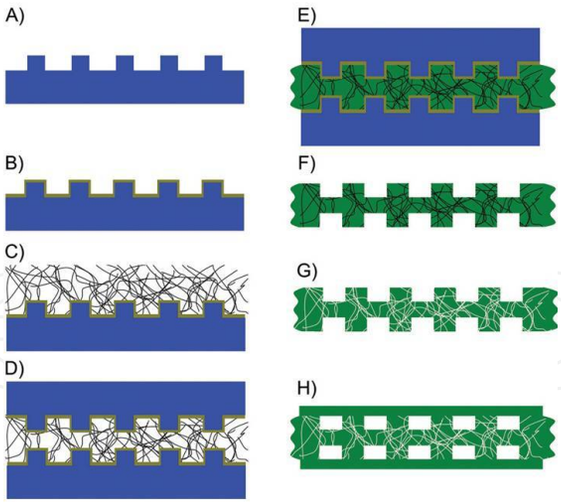

Figure 19. Illustration of hybrid device assembly process. A) A conapoxy mold is patterned from a silicone master. B) The conapoxy mold is coated with a thin layer of sugar. C) A melt-spun sugar microfiber network is adhered to the sugar layer on the conapoxy mold. D) A second sugar-coated conapoxy mold is placed on top of the microfiber network. E) The space between the two conapoxy molds is infiltrated with uncured PDMS. F) When the PDMS has cured, the conapoxy molds are removed. G) The device is placed in a water bath to remove all sugar structures. H) The top and bottom of the channel system are sealed using flat slabs of PDMS.

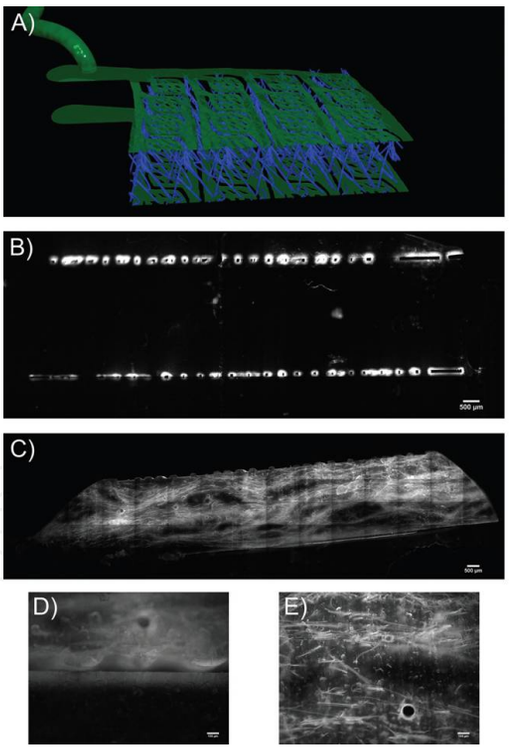

Figure 20. A) Illustration of hybrid device architecture, showing two lithographically patterned channel systems (green) connected by a 3D microfluidic network (blue) formed with sacrificial microfibers. B-D) Fluorescence microscopy images of cross-sections of devices that have been exposed to Rhodamine B dye for 45 minutes. B) A conventional two-layer microfluidic device. C) A hybrid microfluidic device containing both conventionally patterned channels and a microfiber-formed 3D channel network. D,E) Higher magnification images of a hybrid device.

reproduce the *in vivo* flow properties to achieve a physiologically realistic organ mimic. This method is rapid, inexpensive, easily scalable, and requires no toxic materials and therefore enables significant advancements in biomaterials and cell-based biosensor development. However, to produce fully biomimetic scaffolds, it must eventually be adapted for use with hydrogels and we have already made significant progress in this arena.

In collaboration with Dr. Michael Shuler's laboratory at Cornell University, we have developed a micro cell culture analog (μCCA) with 3D hydrogel-cell cultures that reproduces multi-organ interactions and enables chemical toxicity studies in a more physiologically relevant environment [41, 42]. Specific organ cell-hydrogel cultures (liver, marrow, or tumor) are maintained as discrete populations but are connected by channels mimicking blood flow within the device. The fluidic pattern of channels is precisely calculated so that upon fabrication of the chip, the resulting fluid flow mimics the properties of circulating blood. From previous studies, the μCCA was used to observe the physiological effects of naphthalene, doxorubicin, and Tegafur, which all have metabolism-dependent toxicity effects in the body [7, 41, 43]. This microfluidic network enables an accurate physical representation of pharmacokinetic-pharmacodynamic (PK-PD) models for PK profile studies of a compound (*e.g.*, toxicant, pharmaceutical, drug candidate, etc.) [44]. The body's organ systems are accurately represented as individual compartments connected by a "vascular system" of networked fluidic channels. This physical tool allows for the testing of the PK mathematical modeling that predicts the concentration and metabolite profiles of a drug from a given dose [45]. In contrast to PK, the PD of a compound relates to the pharmacological effect of that substance at a given concentration. The time course of pharmacological effects of a substance (at one concentration) can be predicted by combining the PK and PD models [46]. Our advancements of the μCCA have integrated a microfluidic system and a PK-PD modeling approach into an *in vitro/in silico* system that allows for the comparison of physical effects and mathematical predictions in order to generate a more realistic prediction of the toxicity or efficacy of a drug compound (Figure 21) [47].

The multilayered μCCA device is assembled between an aluminum frame and a plexiglass top that seals the PDMS layer that contain the fluidic channel features to a silicon gasket (0.2 mm thick) with cell culture reservoirs (Figure 21A). A polycarbonate base and an additional silicone gasket (0.5 mm thick) are also included to improve sealing of the device. The PDMS fluidic channels mimic the distributed blood flow volume observed *in vivo* for the organ systems represented on the μCCA device: liver (58%), tumor (18%) and marrow (24%) as determined by the PBPK model (Figure 21B) [41, 48]. The cell lines chosen are HepG2-C3A (liver), HCT-116 (colon cancer tumor), myeloblasts Kasumi-1 (marrow), and each population is encapsulated its own hydrogel matrix (alginate or Matrigel™). Figure 21C shows the assembled device.

As an alternative to a peristaltic pump-induced recirculation [41], we adapted the μCCA system to be a pumpless device that functions using gravity-induced flow (Figure 22A) [42]. The pumpless operation eliminates troublesome bubbles that can form and get trapped within the device channels due to use of a peristaltic pump. As shown in Figure 22B, the flow rate is linearly proportional to the height difference. However, the finite size of the reservoir likely explains why the line does not extrapolate to zero. In assembled, rocking μCCA devices, cell survivability was maintained for at least three days without replacement of the medium, but

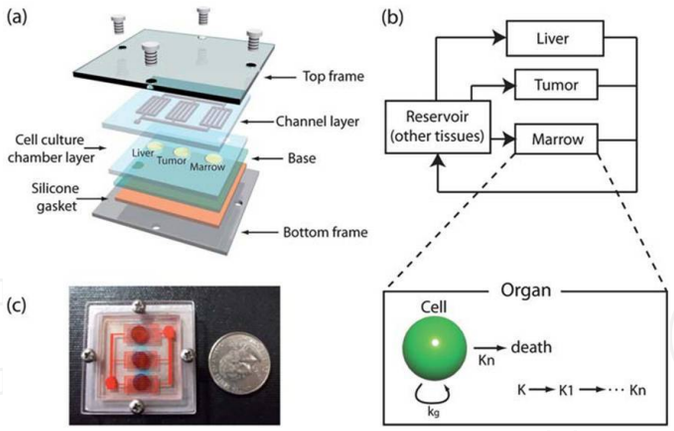

Figure 21. (a) A schematic of device components. A fluidic channel layer and a cell culture chamber layer are superimposed and sealed by top and bottom frames. A silicone gasket and a polycarbonate base are inserted for sealing. (b) A corresponding PBPK model, with the liver, tumor and marrow compartment. Below is a PD model for cell death in each compartment. Although not drawn explicitly, a PD model for each compartment exists separately, and the 'organ' can be the liver, tumor or marrow. (c) A picture of the assembled device. A red dye was used for visualization of channels, and a blue dye was mixed with the alginate. Reproduced by permission of The Royal Society of Chemistry.

viability was extended for a longer time (5 days) with regular changes of medium. For testing, the device was placed on a rocking platform with a directional change occurring every three minutes. The desired concentrations of the drug compound tested, 5-fluorouracil (5-FU) with/without uracil, was added to the cell culture medium, and after the determined exposure time, the device was disassembled for viability staining of the cells (details given in [42]).

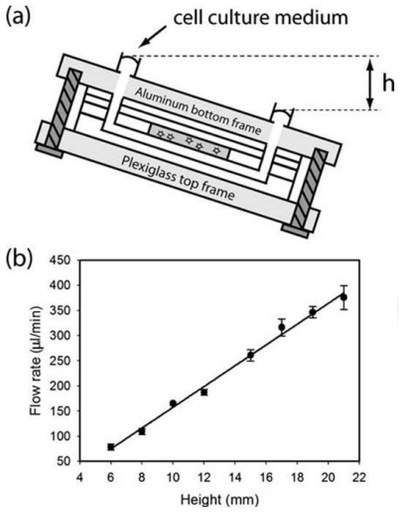

Figure 22. (a) Medium recirculation with gravity-induced flow in a mCCA. Tilting of the device causes liquid to flow from one well to the other well. In about 3 min, the rocking platform changes the angle and medium flows in the opposite direction. (b) A plot of measured flow rates against various heights. Reproduced by permission of The Royal Society of Chemistry.

The chosen cells (liver, tumor and marrow), encapsulated in a hydrogel matrix (alginate or Matrigel), were tested following a three day exposure to 5-FU (0.1 mM) in the presence or

absence of uracil (0.5 mM) (Figure 23). The metabolism of 5-FU, a chemotherapeutic, is inhibited by uracil due to competition for the enzyme (DPD) that primarily metabolizes 5-FU [49, 50]. The addition of uracil allows more 5-FU to remain, and since 5-FU is toxic to cells over time, this combination should prove more toxic to the cell populations. In the case of cells encapsulated in alginate, the viabilities were not statistically different (Figure 23A). However, for the Matrigel-encapsulated cells, the tumor and marrow cells showed a significant decrease in viability with the addition of uracil (Figure 23B). Although both hydrogels are biologically compatible, they likely have different effects on the metabolic activity of the embedded cells. Cells do not readily attach to and remodel alginate because it is a negatively charged polymer, lacking functional groups that facilitate cell signaling and functioning [51]. Matrigel, a protein mixture secreted by Engelbreth-Holm-Swarm (EHS) mouse sarcoma cells, may be more suitable for eukaryotic cells to maintain their functionality and thus their toxicity response, as reported for hepatocytes [52, 53]. This may explain the viability differences we observed between the hydrogels for the cell lines tested, and this remains an area of active research.

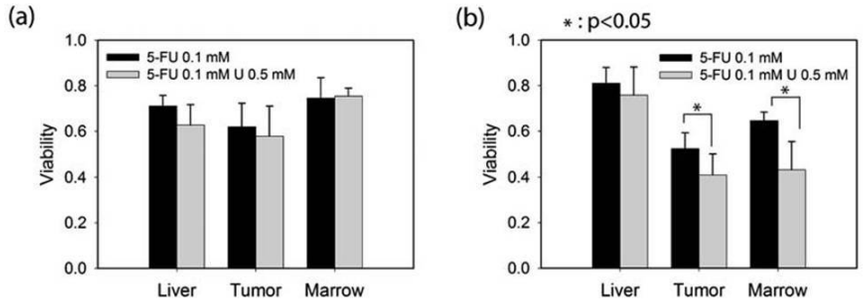

Figure 23. (a) Viability of three cell lines after 3-day treatment with 5-FU alone or 5-FU plus uracil (U) in a μCCA, encapsulated in 2% alginate. (b) Viability of three cell lines after 3-day treatment with 5-FU alone or 5-FU plus uracil (U). Cells were encapsulated in Matrigel™ in a μCCA. Reproduced by permission of The Royal Society of Chemistry.

The simplification of this rocking μCCA system lessens the requirement for specialized techniques for assembly and operation often an issue with microfluidics. We have preserved the ability to perform pharmacokinetic-based toxicity testing on multiple cell types as 3D cell-hydrogel cultures. Further, our research indicates that the physical assembly of the biosensor can be performed without significant cell damage. This supports the use of this type of cell-based biosensor for the use in toxicity monitoring applications.

4. Conclusions

We believe that the work detailed in the above sections provides key technologies and tools that bring us closer to the realization of a total "body on a chip" for applications ranging from pharmaceutical testing of drug candidates to fieldable devices that are capable of physiologically accurate toxicity responses. Additionally, the technologies developed are pursuant toward increasing the cell lifetime and survivability in the biosensor constructs. Since our focus is on military applications, a robust toxicity microanalysis system has innumerable potential

uses for the soldier including toxicity devices for water resources in harsh environments, monitoring at military installations to ensure environmental sustainability, rapid screening of drinking water, and enhanced decision processing for military bases.

Acknowledgements

We would like to thank all of our collaborating academic laboratories who participated in the "In Silico Biomimetic Sensor for Rapid Testing of Water Resources" 6.2 Research Program: those represented in this chapter include Dr. Scott Banta, Columbia University; Dr. Charles Henry, Colorado State University; Dr. Ali Khademhosseini, Harvard University; Dr. Robert Langer, Massachusetts Institute of Technology; Dr. Michael Shuler, Cornell University; as well as those equally important but not described here including Dr. Paul Bohn, University of Notre Dame; Dr. William van der Schalie, U.S. Army Center for Environmental Health Research; and Dr. Yingxiao Wang, University of Illinois at Urbana-Champaign. Additional thanks goes to numerous post-doctoral researchers from those laboratories who also participated in this program. This ERDC-CERL program was supported by funds from the Army Direct Research Program.

Author details

Jill M. Grimme[1] and Donald M. Cropek[1,2*]

*Address all correspondence to: Donald.M.Cropek@usace.army.mil

1 U.S. Army Corps of Engineers, Engineer Research and Development Center – Construction Engineering Research Laboratory, Champaign, IL, USA

2 Department of Veterinary Biosciences, University of Illinois at Urbana-Champaign, Urbana, IL, USA

References

[1] Banerjee, P., Franz, B., and Bhunia, A. K. (2010) Mammalian cell-based sensor system, *Adv Biochem Eng Biotechnol*, *117*, 21-55.

[2] Wang, P. (2010) Introduction, In *Cell-Based Biosensors Principles and Applications* (Wang, P., and Liu, Q., Eds.), pp 1-12, Artech House, Norwood, MA.

[3] Sweeney, L. M., Shuler, M. L., Babish, J. G., and Ghanem, A. (1995) A cell culture analogue of rodent physiology: Application to naphthalene toxicology, *Toxicology in Vitro*, *9*, 307-316.

[4] Baxter, G. T., and Freedman, R. (2004) A Dynamic In Vivo Surrogate Assay Platform for Cell-Based Studies, *Am Biotechnol Lab*, 1-2.

[5] Sin, A., Chin, K. C., Jamil, M. F., Kostov, Y., Rao, G., and Shuler, M. L. (2004) The design and fabrication of three-chamber microscale cell culture analog devices with integrated dissolved oxygen sensors, *Biotechnol Prog*, *20*, 338-345.

[6] Esch, M. B., Sung, J. H., and Shuler, M. L. (2010) Promises, challenges and future directions of microCCAs, *J Biotechnol*, *148*, 64-69.

[7] Viravaidya, K., Sin, A., and Shuler, M. L. (2004) Development of a microscale cell culture analog to probe naphthalene toxicity, *Biotechnol Prog*, *20*, 316-323.

[8] Viravaidya, K., and Shuler, M. L. (2004) Incorporation of 3T3-L1 cells to mimic bioaccumulation in a microscale cell culture analog device for toxicity studies, *Biotechnol Prog*, *20*, 590-597.

[9] McAuliffe, G. J., Chang, J. Y., Glahn, R. P., and Shuler, M. L. (2008) Development of a gastrointestinal tract microscale cell culture analog to predict drug transport, *Mol Cell Biomech*, *5*, 119-132.

[10] Mahler, G. J., Esch, M. B., Glahn, R. P., and Shuler, M. L. (2009) Characterization of a gastrointestinal tract microscale cell culture analog used to predict drug toxicity, *Biotechnol Bioeng*, *104*, 193-205.

[11]

[12] Mahler, G. J., Shuler, M. L., and Glahn, R. P. (2009) Characterization of Caco-2 and HT29-MTX cocultures in an in vitro digestion/cell culture model used to predict iron bioavailability, *J Nutr Biochem*, *20*, 494-502.

[13] Wu, J., Park, J. P., Dooley, K., Cropek, D. M., West, A. C., and Banta, S. (2011) Rapid development of new protein biosensors utilizing peptides obtained via phage display, *PLoS One*, *6*, e24948. http://www.plosone.org/article/fetchArticle.action?articleURI=info:doi/10.1371/journal.pone.0024948

[14] Wu, J., Cropek, D. M., West, A. C., and Banta, S. (2010) Development of a troponin I biosensor using a peptide obtained through phage display, *Anal Chem*, *82*, 8235-8243.

[15] Park, J. P., Cropek, D. M., and Banta, S. (2010) High affinity peptides for the recognition of the heart disease biomarker troponin I identified using phage display, *Biotechnol Bioeng*, *105*, 678-686.

[16] Pumera, M., Merkoci, A., and Alegret, S. (2007) Carbon nanotube detectors for microchip CE: comparative study of single-wall and multiwall carbon nanotube, and

graphite powder films on glassy carbon, gold, and platinum electrode surfaces, *Electrophoresis*, *28*, 1274-1280.

[17] Shiddiky, M. J., Won, M. S., and Shim, Y. B. (2006) Simultaneous analysis of nitrate and nitrite in a microfluidic device with a Cu-complex-modified electrode, *Electrophoresis*, *27*, 4545-4554.

[18] Tang, D. Y., and Xia, B. Y. (2008) Electrochemical immunosensor and biochemical analysis for carcinoembryonic antigen in clinical diagnosis, *Microchim Acta*, *163*, 41-48.

[19] Sameenoi, Y., Mensack, MM., Boonsong, K., Ewing, R., Dungchai, W., Chailapakul, O., Cropek, DM., Henry, CS. (2011) Poly(dimethylsiloxane) cross-linked carbon paste electrodes for microfluidic electrochemical sensing, *Analyst*, *136*, 3177-3184. http://pubs.rsc.org/en/content/articlelanding/2011/an/c1an15335h

[20] Bayle, C., Causse, E., and Couderc, F. (2004) Determination of aminothiols in body fluids, cells, and tissues by capillary electrophoresis, *Electrophoresis*, *25*, 1457-1472.

[21] Pastore, A., Federici, G., Bertini, E., and Piemonte, F. (2003) Analysis of glutathione: implication in redox and detoxification, *Clin Chim Acta*, *333*, 19-39.

[22] Pereira-Rodrigues, N., Cofre, R., Zagal, J. H., and Bedioui, F. (2007) Electrocatalytic activity of cobalt phthalocyanine CoPc adsorbed on a graphite electrode for the oxidation of reduced L-glutathione (GSH) and the reduction of its disulfide (GSSG) at physiological pH, *Bioelectrochemistry*, *70*, 147-154.

[23] Korfhage, K. M., Ravichandran, K., and Baldwin, R. P. (1984) Phthalocyanine-containing chemically modified electrodes for electrochemical detection in liquid chromatography/flow injection systems, *Analytical Chemistry*, *56*, 1514-1517.

[24] Halbert, M. K., and Baldwin, R. P. (1985) Electrocatalytic and analytical response of cobalt phthalocyanine containing carbon paste electrodes toward sulfhydryl compounds, *Analytical Chemistry*, *57*, 591-595.

[25] Kuhnline, C. D., Gangel, M. G., Hulvey, M. K., and Martin, R. S. (2006) Detecting thiols in a microchip device using micromolded carbon ink electrodes modified with cobalt phthalocyanine, *Analyst*, *131*, 202-207.

[26] Du, M., Flanigan, V., and Ma, Y. (2004) Simultaneous determination of polyamines and catecholamines in PC-12 tumor cell extracts by capillary electrophoresis with laser-induced fluorescence detection, *Electrophoresis*, *25*, 1496-1502.

[27] Westerink, R. H. (2004) Exocytosis: using amperometry to study presynaptic mechanisms of neurotoxicity, *Neurotoxicology*, *25*, 461-470.

[28] Chen, T. K., Luo, G., and Ewing, A. G. (1994) Amperometric monitoring of stimulated catecholamine release from rat pheochromocytoma (PC12) cells at the zeptomole level, *Anal Chem*, *66*, 3031-3035.

[29] Kozminski, K. D., Gutman, D. A., Davila, V., Sulzer, D., and Ewing, A. G. (1998) Voltammetric and pharmacological characterization of dopamine release from single exocytotic events at rat pheochromocytoma (PC12) cells, *Anal Chem*, *70*, 3123-3130.

[30] Li, M. W., Spence, D. M., and Martin, R. S. (2005) A microchip-based system for immobilizing PC 12 cells and amperometrically detecting catecholamines released after stimulation with calcium, *Electroanalysis*, *17*, 1171-1180.

[31] Aubin, H., Nichol, J. W., Hutson, C. B., Bae, H., Sieminski, A. L., Cropek, D. M., Akhyari, P., and Khademhosseini, A. (2010) Directed 3D cell alignment and elongation in microengineered hydrogels, *Biomaterials*, *31*, 6941-6951. http://www.sciencedirect.com/science/article/pii/S0142961210006939

[32] Kim, S. B., Bae, H., Cha, J. M., Moon, S. J., Dokmeci, M. R., Cropek, D. M., and Khademhosseini, A. (2011) A cell-based biosensor for real-time detection of cardiotoxicity using lensfree imaging, *Lab Chip*, *11*, 1801-1807. http://pubs.rsc.org/en/content/articlelanding/2011/lc/c1lc20098d

[33] Charest, J. L., Eliason, M. T., Garcia, A. J., and King, W. P. (2006) Combined microscale mechanical topography and chemical patterns on polymer cell culture substrates, *Biomaterials*, *27*, 2487-2494.

[34] Brammer, K. S., Oh, S., Cobb, C. J., Bjursten, L. M., van der Heyde, H., and Jin, S. (2009) Improved bone-forming functionality on diameter-controlled TiO(2) nanotube surface, *Acta Biomater*, *5*, 3215-3223.

[35] Charest, J. L., Garcia, A. J., and King, W. P. (2007) Myoblast alignment and differentiation on cell culture substrates with microscale topography and model chemistries, *Biomaterials*, *28*, 2202-2210.

[36] Boheler, K. R., Czyz, J., Tweedie, D., Yang, H. T., Anisimov, S. V., and Wobus, A. M. (2002) Differentiation of pluripotent embryonic stem cells into cardiomyocytes, *Circ Res*, *91*, 189-201.

[37] Stummann, T. C., Wronski, M., Sobanski, T., Kumpfmueller, B., Hareng, L., Bremer, S., and Whelan, M. P. (2008) Digital movie analysis for quantification of beating frequencies, chronotropic effects, and beating areas in cardiomyocyte cultures, *Assay Drug Dev Technol*, *6*, 375-385.

[38] Vandecasteele, G., Eschenhagen, T., Scholz, H., Stein, B., Verde, I., and Fischmeister, R. (1999) Muscarinic and beta-adrenergic regulation of heart rate, force of contraction and calcium current is preserved in mice lacking endothelial nitric oxide synthase, *Nat Med*, *5*, 331-334.

[39] Xiao, L., Hu, Z., Zhang, W., Wu, C., Yu, H., and Wang, P. (2010) Evaluation of doxorubicin toxicity on cardiomyocytes using a dual functional extracellular biochip, *Biosens Bioelectron*, *26*, 1493-1499.

[40] Bellan, L. M., Singh, S. P., Henderson, P. W., Porri, T. J., Craighead, H. G., and Spector, J. A. (2009) Fabrication of an artificial 3-dimensional vascular network using sacrificial sugar structures, *Soft Matter*, *5*, 1354-1357.

[41] Bellan, L. M., Kniazeva, T., Kim, E. S., Epshteyn, A. A., Cropek, D. M., Langer, R., and Borenstein, J. T. (2012) Fabrication of a hybrid microfluidic system incorporating both lithographically patterned microchannels and a 3D fiber-formed microfluidic network, *Adv Healthc Mater*, *1*, 164-167. http://onlinelibrary.wiley.com/doi/10.1002/adhm.201290009/abstract

[42] Sung, J. H., and Shuler, M. L. (2009) A micro cell culture analog (microCCA) with 3-D hydrogel culture of multiple cell lines to assess metabolism-dependent cytotoxicity of anti-cancer drugs, *Lab Chip*, *9*, 1385-1394.

[43] Sung, J. H., Kam, C., and Shuler, M. L. (2010) A microfluidic device for a pharmacokinetic-pharmacodynamic (PK-PD) model on a chip, *Lab Chip*, *10*, 446-455. http://pubs.rsc.org/en/content/articlelanding/2010/lc/b917763a

[44] Tatosian, D. A., Shuler, M. L., and Kim, D. (2005) Portable in situ fluorescence cytometry of microscale cell-based assays, *Opt Lett*, *30*, 1689-1691.

[45] Gerlowski, L. E., and Jain, R. K. (1983) Physiologically based pharmacokinetic modeling: principles and applications., *J Pharm Sci*, *72*, 1103-1127.

[46] Ghanem, A., and Shuler, M. L. (2000) Combining cell culture analogue reactor designs and PBPK models to probe mechanisms of naphthalene toxicity, *Biotechnol Prog*, *16*, 334-345.

[47] Derendorf, H., and Meibohm, B. (1999) Modeling of pharmacokinetic/pharmacodynamic (PK/PD) relationships: concepts and perspectives, *Pharm Res*, *16*, 176-185.

[48] Sung, J. H., and Shuler, M. L. (2009) In *Methods in Bioengineering: Microdevices in Biology and Medicine* (Nahmias, Y., and Bhatia, S., Eds.), Artech House.

[49] Davies, B., and Morris, T. (1993) Physiological parameters in laboratory animals and humans, *Pharm Res*, *10*, 1093-1095.

[50] Van Kuilenburg, A. B., Meinsma, R., Zoetekouw, L., and Van Gennip, A. H. (2002) Increased risk of grade IV neutropenia after administration of 5-fluorouracil due to a dihydropyrimidine dehydrogenase deficiency: high prevalence of the IVS14+1g>a mutation, *Int J Cancer*, *101*, 253-258.

[51] de Bono, J., and Twelves, C. (2001) The oral fluorinated pyrimidines., *Invest New Drugs*, *19*, 41-59.

[52] Lawson, M. A., Barralet, J. E., Wang, L., Shelton, R. M., and Triffitt, J. T. (2004) Adhesion and growth of bone marrow stromal cells on modified alginate hydrogels, *Tissue Eng*, *10*, 1480-1491.

[53] Brandon, E. F., Raap, C. D., Meijerman, I., Beijnen, J. H., and Schellens, J. H. (2003) An update on in vitro test methods in human hepatic drug biotransformation research: pros and cons, *Toxicol Appl Pharmacol*, *189*, 233-246.

[54] Castell, J. V., and Gomez-Lechon, M. J. (2009) Liver cell culture techniques, *Methods Mol Biol*, *481*, 35-46.

IntechOpen